Impact-Induced Delamination in $[0_5, 90_5, 0_5]$ Carbon Fiber/Polyetheretherketone Composite Laminates

HAO WANG *and* TOAN VU-KHANH*

Ecole Polytechnique de Montréal
Montréal, Québec, Canada

National Research Council Canada
Industrial Materials Institute
Boucherville, Québec, Canada J4B 6Y4

This paper reports both experimental and numerical investigations on delamination mechanisms in $[0_5, 90_5, 0_5]$ carbon fiber(CF)/poly(etheretherketone) (PEEK) laminate subjected to low-velocity impact. It was found that the CF/PEEK composite exhibits the same damage mechanisms as epoxy-based composites, but superior delamination resistance. For the crossply laminate, the impact delamination results from a Mode II interlaminar fracture process, and a close association exists between the interlaminar shear stress field and the delamination growth. The prediction of impact-induced delamination sizes is discussed.

INTRODUCTION

Laminated composites are inherently susceptible to internal damage caused by low-velocity impact of foreign objects (1). Impact-induced delamination is identified as the predominant damage mode which may escape visual inspection but can cause a significant reduction in the residual compressive strength of composite structures (2, 3). Numerous experimental and analytical investigations have been conducted to study the impact response and damage mechanisms of composite laminates, but prediction of the impact delamination is still impossible.

Physically, the impact delamination results from a dynamic fracture process of crack initiation, propagation and arrest at the interface between two layers of different orientations. Transverse matrix cracks within layers are found to control the delamination initiation (4-7). These cracks occur early during impact and cause stress concentrations at the interface, from which the delamination is initiated. After initiation, the delamination has a rapid unstable growth and subsequent arrest within a short duration (8). The arrested delamination is generally a 'peanut shape' area at the interface, which becomes larger when the interface is nearer to the non-impacted surface of the laminate. The major axis of the 'peanut shape' delamination is oriented in the fiber direction of the lower layer (9-11).

The impact stress field in a laminate seems to consist of two parts which result respectively from the local contact deformation and the plate bending deformation (12, 13). Analyses of laminate beams (5, 6, 14) show that the contact stress field is localized near the contact zone and is responsible for initiating the delamination by producing transverse matrix cracks. Just outside of the contact zone, the plate bending stress field resumes and acts in an area where the delamination propagates and is arrested. The laminate plate theory has been applied for modeling the low-velocity impact response of composite laminates (15-18).

High performance thermoplastic composites such as carbon fiber/poly(etheretherketone) (CF/PEEK) are being favorably considered for structural applications since the thermoplastic matrix exhibits much higher toughness than a thermoset matrix. The matrix failure modes such as matrix cracking and delamination are effectively reduced (19, 20).

In the present work, experimental investigations are carried out on the low-velocity impact delamination of CF/PEEK laminates. The mechanism of impact damage in this material is analyzed and compared to that reported in the literature for other comosite systems. Prediction of delamination sizes in laminated composites under impact is discussed.

EXPERIMENTAL PROCEDURE

Specimen Fabrication

All samples were compression molded from the CF(AS4)/PEEK matrix thermoplastic composite,

---

*To whom correspondence should be addressed.

APC-2. The recommended molding cycle (21) was followed, which resulted in a crystallinity of about 31%. Square plates 152.4 by 152.4 mm were molded with $[0_5, 90_5, 0_5]$ stacking sequence. The nominal thickness was 2.1 mm. This laminate type was selected because it has been studied extensively for impact response and damage mechanisms in other composite materials [5, 8, 22–24].

In order to analyze the fracture surfaces of the Mode I and Mode II interlaminar fracture under impact load, end-notched beam specimens with $[0_{13}, 90, 0_{13}]$ layup were prepared with the dimensions 152.4 mm long, 25.4 mm wide, and 3.8 mm thick. A strip of Kapton film, 25 μm thick, was inserted between one of the 0/90 interfaces during layup to provide a 35 mm precrack at one end.

Impact Test and Damage Detection

The impact tests were conducted on a Dynatup-8200 drop weight tester. The instrumented data acquisition system provide a digitized record of the impact force history. The impactor mass was 1.27 kg.

In testing the plate specimens, each sample was clamped around its four edges by a couple of steel holders mounted on the base of the tester (*Fig. 1*), leaving a test section of 128 by 128 mm. Since the buckling-related delamination growth (25) is beyond the scope of the study, reverse bending of the plate should be suppressed to prevent this mechanism. A grid-shaped steel frame was attached to the top holder, and eight screws were placed in the frame to provide local constraints to reverse bending, see *Fig. 1*. Actually, each screw was adjusted to give about 0.5 mm spacing before touching the plate surface, because a small reverse bending may occur at the beginning of impact (24). The steel impactor used in the test had a hemispherical nose of 12.7 mm in diameter. The impact velocities were between 1.25 and 3.97 m/s, giving an impact energy range of 1 to 10 J which would result in damage states ranging from delamination initiation to its full growth to the clamped edges. The impact force history was recorded for numerical analysis.

After impact, the plates were subjected to penetrant-enhanced X-radiography, and those with extensive delaminations were unstacked by the thermal deply technique (10, 11, 26). Tetrabromoethane (TBE) was used as the X-ray opaque penetrant and ether solution of gold chloride as the dye-agent in deply. Five small holes, 0.5 or 1.0 mm in diameter, were drilled at and around the impact point to help penetration of these agents into the damaged area. Though destructive in nature, neither the drilling nor deplying process caused considerable change to the delamination size.

A line-nosed impactor, also 12.7 mm in diameter, was used for the impact fracture of beam specimens (*Fig. 2*). 10 to 12 J impact energy was used to initiate both Mode I and Mode II delaminations.

After impact, each beam was opened and the delamination surface was examined under the scanning electron microscope (SEM). The impact delamination surfaces of several plate specimens were also examined by SEM in order to identify the failure mechanism.
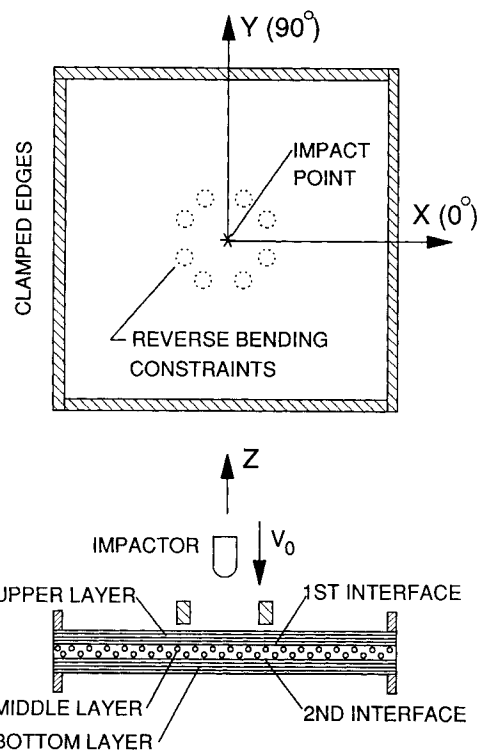

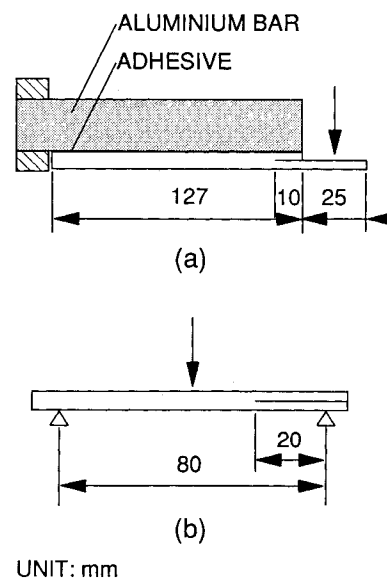Fig. 1. Impact test of $[0_5, 90_5, 0_5]$ CF/PEEK Laminates.

UNIT: mm

Fig. 2. Impact fracture tests of end-notched beams: (a) Mode I; (b) Mode II.

EXPERIMENTAL RESULTS

Impact Response

Figure 3 shows the impact force history of a laminate subjected to 5 J impact. The contact between the impactor and laminate lasted about 5.44 ms and a maximum load of 2.12 kN was attained at approximately half of the contact duration. A small amplitude signal with higher frequencies was found superimposed on the basic load curve. This signal seems related to the damage growth during contact (27). For energy levels up to 7 J, this signal ceased when unloading began, possibly implying that the major damage growth finished at the time of the maximum load. At 10 J impact, this signal might cease a short time after the maximum load. Also plotted in the figure is the laminate deflection at the impact point, as integrated from the load-time signal for the mass of the impactor used. It is seen that the impact event finished before reverse bending of the plate began. Thus, suppressing the reverse bending did not affect the impact event, and it is reasonable to assume that the damage growth occurred only during the impact duration.

Delamination Characterization

Figure 4 shows the damage pattern of a square laminate after 5 J impact. Transverse matrix cracking and delamination were the primary damage modes. No fiber breakage was found in the specimen surfaces. At the impact site, however, a shallow circular impression due to impactor indentation was observed. The diameter of such an impression is less than 6 mm for the energy levels up to 7 J, and is much smaller than the impact damage sizes. At 10 J impact energy, it increases to 10 mm because the indentation crush occurred in the contact zone.

In *Fig. 5*, the total delamination area, as measured from the overlapped delamination image in the X-ray pictures, is plotted against the impact energy. The previously reported linear dependence was found to be valid (23, 28, 29). Results for the same laminate type but for epoxy-based composites were taken from (29) for comparison. Considering the difference in plate dimensions, the CF/PEEK composite seems more resistant to impact delamination than Kevlar/epoxy and graphite/epoxy composites. Glass/epoxy composite exhibits even better delamination resistance, possibly because of the low stiffness anisotropy of the material (29).

Figure 6 shows the delamination contours at both interfaces of the laminate obtained by the deply technique. These contours, when overlapped, agree with the X-ray picture in *Fig. 4*. The key feature of impact delamination is the 'peanut-shape' area, which is oriented in the fiber direction of the lower ply. This feature permits a consistent characterization of the delamination geometry by defining the length *L* and width *W*, respectively, in the fiber direction of the lower ply and in the corresponding

transverse direction (30), see *Fig. 6*. The delamination sizes at both interfaces are shown in *Fig. 7* against the impact energy. Both delaminations
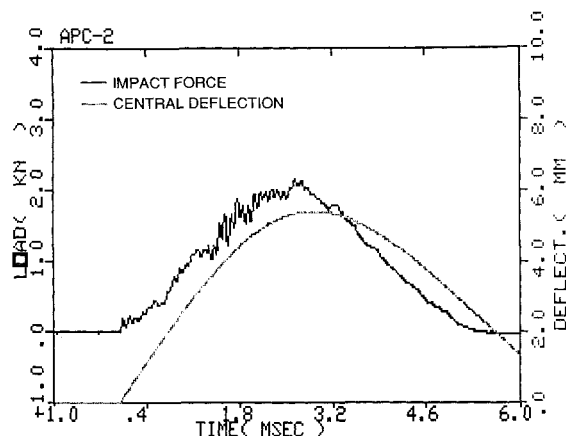

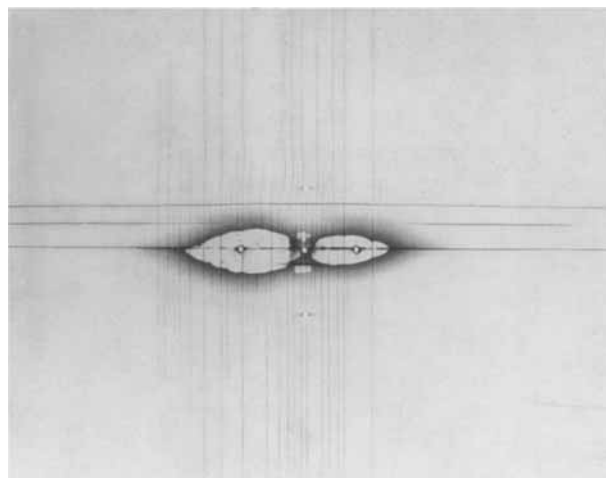Fig. 3. Contact force and central deflection of a plate under impact.

Fig. 4. X-radiography of low-velocity impact damage in a [0_5, 90_5, 0_5] CF/PEEK laminate.
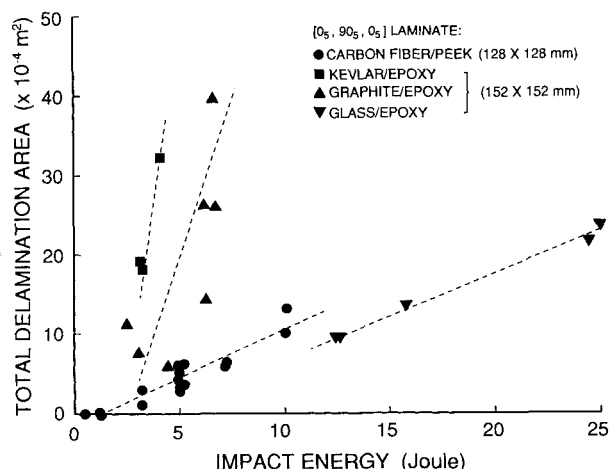

Fig. 5. Total delamination area versus impact energy for three-layer crossply laminates.

(a) 1ST INTERFACE DELAMINATION
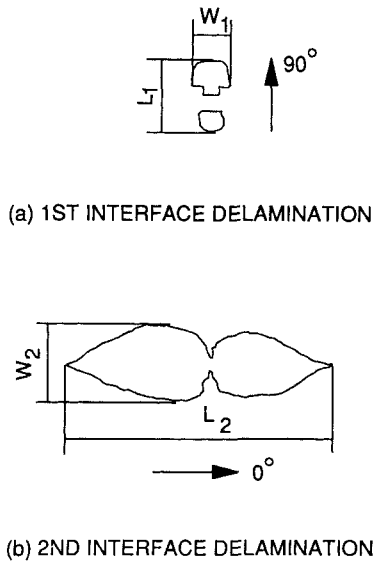

(b) 2ND INTERFACE DELAMINATION

Fig. 6. Delamination geometries at both interfaces of a $[0_5, 90_5, 0_5]$ laminate: (a) first interface; (b) second interface.
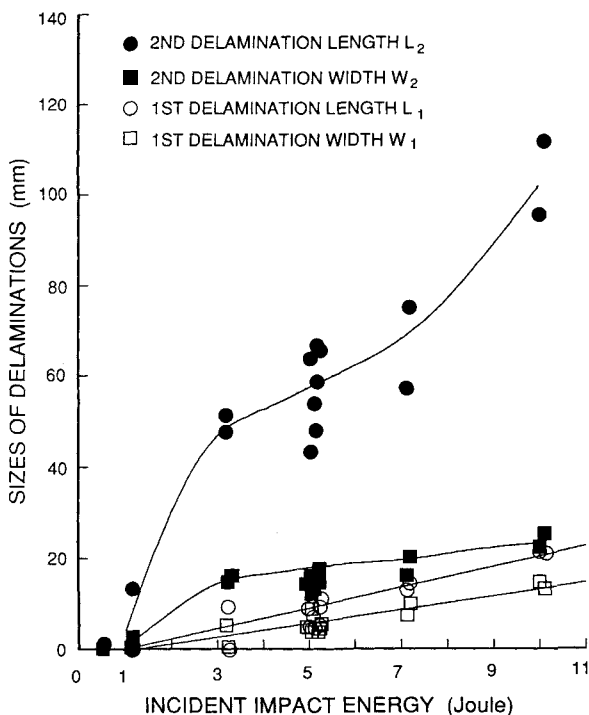

Fig. 7. Sizes of delaminations at both interfaces versus incident impact energy.

were initiated between 1 and 3 J. With the second interface (lower interface) delamination occurred earlier than the first interface (upper interface) delamination. After initiation, the second delamination is always larger than the first. The length of the second delamination, L_2, increases non-linearly with impact energy up to the clamped edges, while its width, W_2, varies only slightly. On the other hand,

the first delamination is premature in all cases, and both its length L_1 and width W_1 vary linearly with impact energy.

Transverse Matrix Cracks

Though transverse matrix cracking is of less concern in the present study, it is important because it can initiate delamination and interact with delamination growth. This is clearly seen in *Fig. 4*. In the upper layer, two major matrix cracks were observed near, but at a certain distance from, the impact point. These cracks may have occurred at the early stage of impact (8). They were produced by the local contact stress field, thus short lengths resulted. The first delamination was initiated along the full length of these cracks to propagate in the 90-degree direction. In the middle layer, two sets of evenly distributed matrix cracks were observed. One set extended across the whole span of the plate, while the other set, the short cracks, were distributed around the second delamination. A close association of the short cracks with the delamination growth is evident. In the bottom layer, a few cross-span transverse cracks occurred. The second delamination always followed one of these cracks to form the pointed ends of its "peanut shape."

Fractography of Delamination Surface

Figs 8(a) and *8(b)* present, respectively, the delamination surface morphologies of the Mode I and Mode II impact fracture tests; *Fig. 8(c)* shows the fracture surface of the impact delamination of plate specimens. These photographs were taken on the 0-degree ply surfaces. The crack propagation direction was from the top towards the bottom. An obvious comment is that the impact delamination surface resembles that of the Mode II fracture, which may possibly be the dominant failure mechanism. For both cases, the delamination surface exhibited shearing deformation of the matrix, with no distinct hackles such as observed in epoxy-based composites (7). However, on the Mode I delamination surface, an ill-defined hackle pattern was observed. These hackles seemed to be formed from the resin-rich region between the fibers.

The above observations seem to suggest that the impact delamination is mainly governed by a shear Mode II fracture. In order to better understand the delamination process, numerical analyses were carried out to calculate the interlaminar shear stresses in these plates.
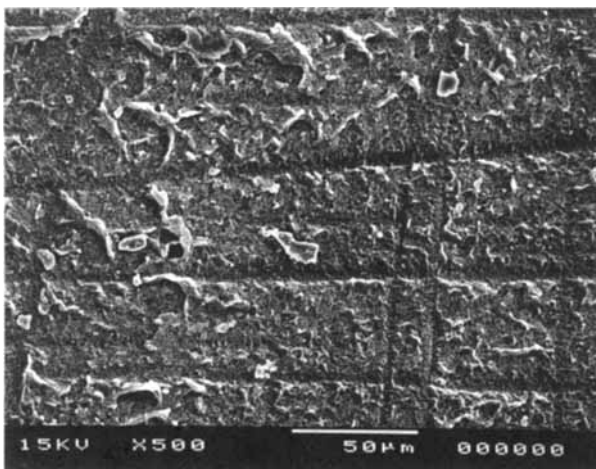
Numerical Model

Transient dynamic finite element analyses were performed using the structural analysis program ABAQUS (31). The problem was simulated as a square plate being impacted at its center by a concentrated force. Plate elements based on the shear deformable laminate theory (32) were employed. The measured impact force history was applied.
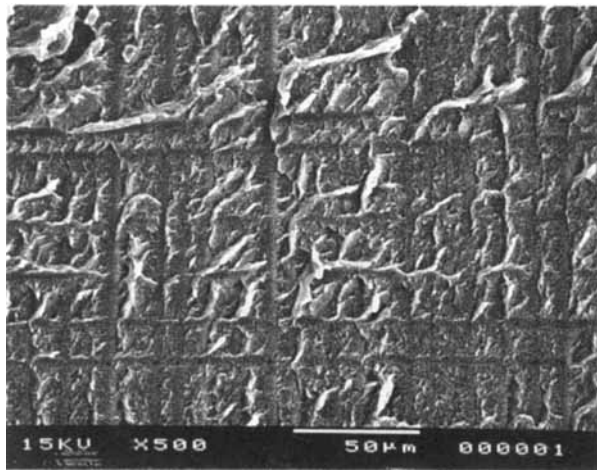
(a)
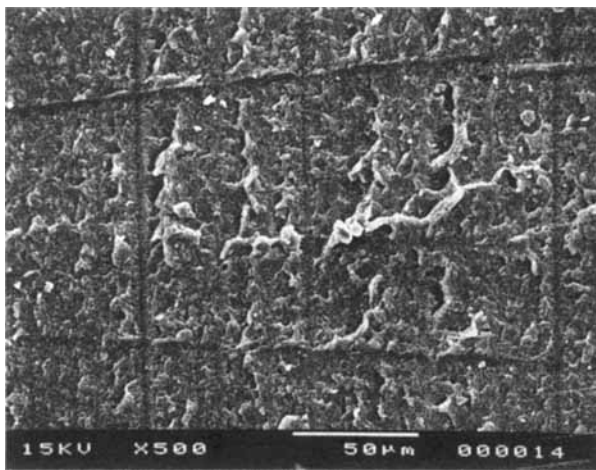
(b)

(c)

Fig. 8. Fracture surface morphologies of 0/90 interface delamination under impact: (a) Mode I; (b) Mode II; (c) impact delamination.

The above modeling neglected the local contact deformation near the impact point. Therefore, it is not valid for the damage initiation phase. For the purpose of the present study, however, the stress field away from the impact point is considered. From the test observations, typical delaminations were much larger than the contact zone. The simplification of a concentrated force should be acceptable if the far-field response is concerned.

Although interlaminar shear stresses are not included in formulating the laminate theory, it is acceptable practice to evaluate their values by integrating the local equilibrium equations through the layer thickness in succession (33, 34). These are

$$\tau_{xz,z} = -(\sigma_{x,x} + \tau_{xy,y}) \qquad (1)$$

$$\tau_{yz,z} = -(\sigma_{y,y} + \tau_{xy,x}) \qquad (2)$$

where σ_x, σ_y and τ_{xy} are the in-plane stresses, τ_{xz} and τ_{yz} are the transverse shear stress components, all defined in the coordinate system shown in *Fig. 1*. Since *Eqs 1* and *2* represent the in-plane equilibrium of a material point which undergoes negligible in-plane movement, both gravity and inertia forces have been dropped. This stress evaluation procedure was included in a post-processing program.

Due to the symmetry conditions, the 8 by 8 nonuniform mesh shown in *Fig. 9* was selected to model a quarter of the square plate. This mesh and the shear stress evaluation procedure were checked by the static problem of Pagano and Hatfield (35). The length/thickness ratio at present is 61. If scaled to 50, the maximum transverse shear stresses were within 5% from the analytical values.

Since elastic wave measurements on similar laminate configurations suggested a flexural wave dominated response (24), a small deflection linear analysis was carried out for the impact duration. The direct time integration scheme based on the Newmark Beta method (36) was employed. For the typical case of 5 J impact, the influence of time step selection on interlaminar shear stresses was examined. Not much difference was observed for the time step range between 10 and 100 μs, so time steps between 20 and 50 μs were used for all the cases.

Due to the high processing temperature and semicrystallinity of the thermoplastic material, significant thermal residual stresses are built up in the laminate (37). This effect was considered by including the residual strains, which were evaluated approximately by the 'first-ply-failure' method and the laminate theory (38). In the transverse direction of both 0 and 90-degree layers, the estimated residual strains are 0.644% and 0.707%, respectively. These values were obtained at the same time as the impact test, i.e. within two weeks after molding.

Finally, in the above analyses, the carbon-fiber/PEEK composite was assumed to be linearly elastic. The following material constants were used in the analysis: $E_{11} = 134$ GPa, $E_{22} = 8.9$ GPa, $G_{12} = 5.1$ GPa, $\nu_{12} = 0.29$, $\rho = 1600$ kg/m³ and $\sigma_y^{cr} = 80$ MPa. These constants were taken from the ICI documentation (39). The preliminary test on material properties gave similar values [21].
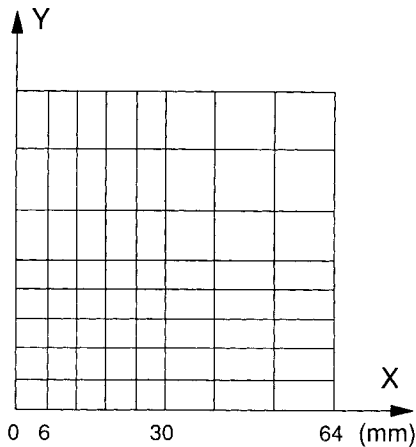
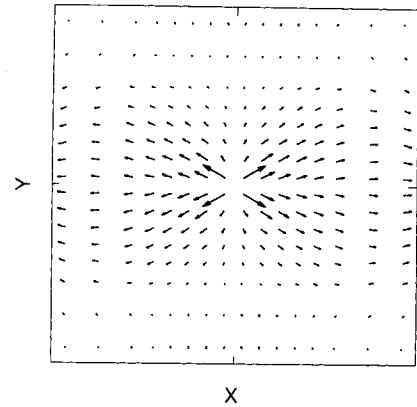Fig. 9. Finite element mesh for a quarter of the square laminate.

Fig. 10. Instant distribution of interlaminar shear stress as a vector field. The length of the vector in the plot is scaled by multiplying a factor of: $f = (\tau_{max}/\tau)^{1/2}$, where τ is the length of a shear stress vector and τ_{max} is the maximum length among all the vectors.

Interlaminar Shear Stress and Delamination Behavior

Owing to the assumptions incorporated in laminate theory, the interlaminar shear stresses are the same at both interfaces of the laminate. This was also observed in the three dimensional analysis (22) except near the impact point.

Figure 10 shows the instant distribution of interlaminar shear stresses as a vector field at the interface plane. The laminate is subjected to a concentrated force simulating 5 J impact. The plot shown at 2200 μs after impact corresponds to the maximum impact force. The stress field exhibits both strong nonuniformity and directionality. A shear stress concentration occurs near the impact point, and the shear stress vectors are more inclined to the x-axis. In the area around the x-axis, where $\tau_{yz} = 0$, a forward shearing in the x-direction predominates. A similar area with forward shearing in the y-direction is also observed around the y-axis, where $\tau_{xz} = 0$. Referring to the test observations in *Fig. 6*, the delaminations at the second and first interfaces occurred within these two areas, as well as in the forward shearing directions, respectively. It is thus believed that both delaminations resulted from a Mode II dominated fracture process. This is in agreement with the fractographic observations as discussed earlier.

The above observation is further clarified by plotting the shear stress field in its two axial components, τ_{xz} and τ_{yz}. Shown in *Fig. 11* are the contour plots of shear stress components at the time of maximum impact force, for different impact energies, respectively. It is seen that, while stress concentrations exist for both components, τ_{xz} exhibits much higher values than τ_{yz} for most of the plate area. In τ_{xz} distribution, a high value region occurs within a narrow strip along the x-axis; and the stress contours within this region exhibit a "peanut shape," which resembles the second interface delamination. Similarly, in τ_{yz} distribution, the high-value con-

tours are around the y-axis and resemble the first interface delamination.

These features of stress distribution can be used to understand the delamination behavior as observed in the test. Because of its initiation from the upper layer matrix cracks, the first delamination propagates in the 90-degree direction under the nominal stress of τ_{yz}. This stress component decreases rapidly along the crack path. Thus, the first delamination is arrested after a short growth. The second delamination, on the other hand, is initiated from the matrix cracks in the middle layer. It propagates in the 0-degree direction, along which τ_{xz} predominates and keeps higher values for a larger extent. A large delamination growth occurs before arrest. Thus, the delamination behavior at a given interface depends not only on the interlaminar shear stresses, but also on the initiation mechanism.

As mentioned earlier, the instant of maximum impact load seems to correspond to the time of delamination arrest. Thus, for comparison purposes, the second delamination length L_2, and width W_2, are compared with the calculated shear stress τ_{xz} contours such as in *Fig. 11*, at various impact energy levels. These are shown in *Figs. 12* and *13* for the length and width, respectively. Surprisingly enough, within the scatter of the experimental measurements, the delamination sizes seem to be governed by a constant interlaminar shear stress. These figures also show that the shear stresses corresponding to the delamination width, W_2, seem to be higher than those corresponding to the delamination length, L_2. This could be understood since a propagation of the delamination in the y-direction under the shear stress field τ_{xz} would be under a Mode III crack propagation. Measurements carried out on graphite/epoxy composites (40) showed that the Mode III delamination energy is higher than that of Mode II. One can, therefore, expect the same tendency in CF/PEEK composite, which results in less delamination in the y-direction. The results also
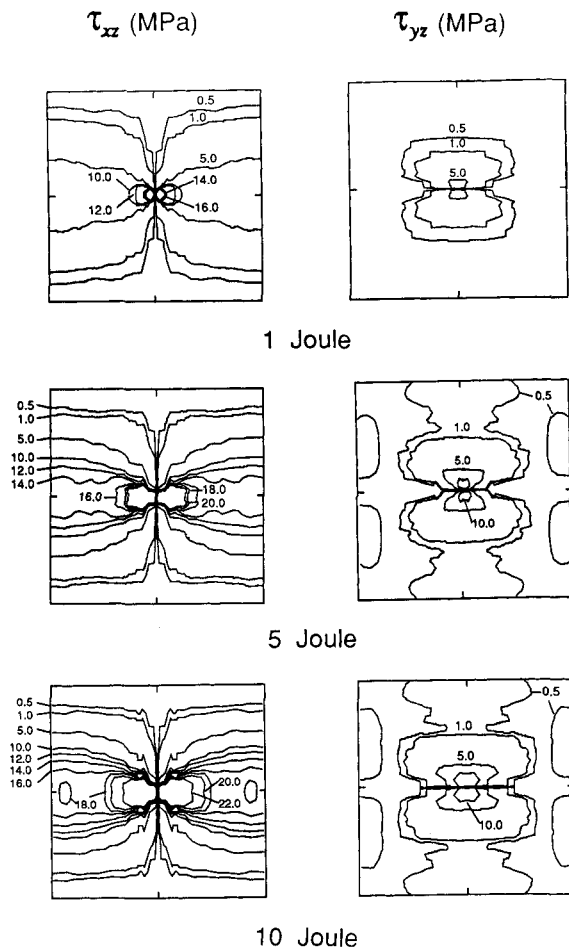
τ_{xz} (MPa) τ_{yz} (MPa)

1 Joule

5 Joule

10 Joule

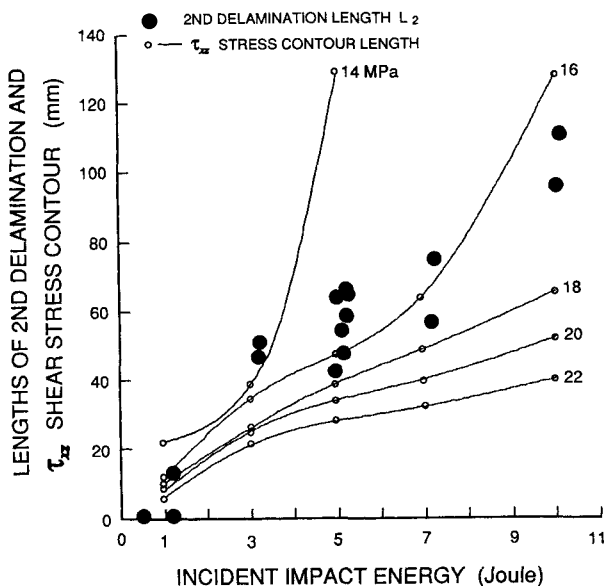Fig. 11. *Interlaminar shear stress contours at the instant of maximum impact load.*

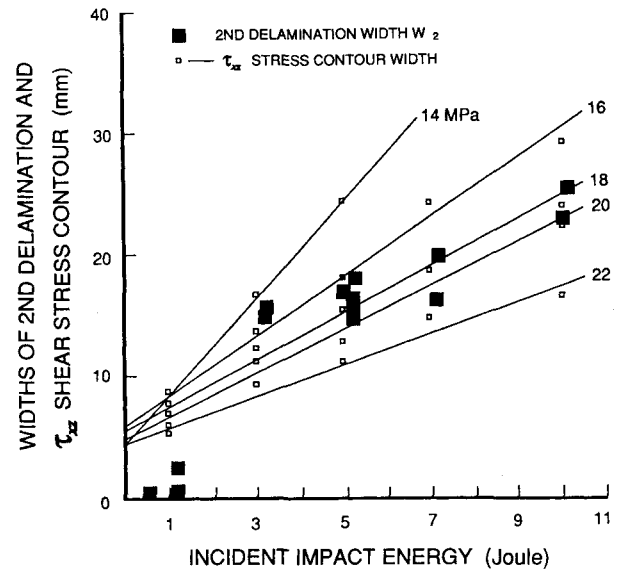Fig. 12. *Correlation between τ_{xz} contour and second interface delamination: length L_2.*

Fig. 13. *Correlation between τ_{xz} contour and second interface delamination: width W_2.*

confirm the predominance of Mode II fracture in the impact delamination process discussed above. It is worth noting that the transverse matrix cracking probably plays an important role in the delamination width. The transverse cracks appear before delamination and, with the stress concentration around these cracks, delamination grows in the x-direction. The width of delamination, W_2, is, therefore, rather controlled by the initiation process of delamination.

For the moment, it is not clear why the shear stress τ_{xz} at the delamination contour remains relatively constant at various levels of impact energy. In fact this value is much lower than the expected interlaminar shear strength of this composite. The impact tests performed on Mode II flexural end notch beam samples suggest that delamination grows in an unstable manner. Since the fracture surface of these samples is close to that of the observed delamination as discussed above, it is reasonable to assume that delamination grows unstably in the x-direction. The parameter which would govern L_2 is, therefore, associated with the crack arrest process.

Much controversy still remains regarding the material parameter controlling the crack arrest. The crack arrest toughness has often been considered as a material constant. Previous work on crack arrest showed that the static strain energy release rate at crack arrest, G_{IIa}, can be measured (41). *Figure 14* presents the static strain energy release rate at crack arrest, G_{IIa}, in a glass/epoxy cross ply laminate. Although the scatter of the results is relatively large, G_{IIa} seems to be a constant. Further work (42) also demonstrated that in these flexural samples, when the crack is not exactly at the mid thickness, fracture occurs under a mixed Mode (I and II). However,
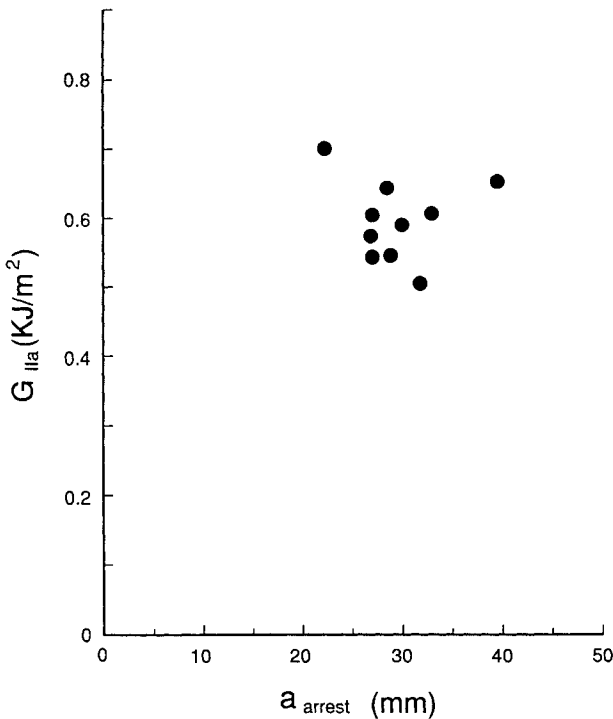
Fig. 14. Arrest toughness (G_{IIa}) in $[90_3/0/90_6/0/90_3]_s$ glass/epoxy laminate.

Fig. 15. Nominal interlaminar shear stress τ_{xz} at second delamination arrest.

as a first attempt to understand the process of impact damage, only Mode II is considered. With this assumption, the above correlation between far field shear stress τ_{xz} and the delamination length L_2 might be explained in terms of crack arrest toughness. It is well known that the stress intensity factor, K_{II}, depends on both the geometry of the sample and the crack length by:

$$K_{II} = Y\tau_0\sqrt{a} \qquad (3)$$

where τ_0 is the nominal shear stress, Y is the geometrical function which also depends on the crack length a. If the crack arrest toughness is a constant, there should be a unique correlation between the nominal shear stress τ_0 and the crack length a for a given sample geometry. *Figure 15* shows the plot of τ_{xz} as a function of the delamination length L_2. Within the scatter of the experimental data, there seems to be a unique relationship between τ_{xz} and L_2, suggesting therefore that the crack arrest toughness could be considered as a material constant which controls the extent of impact delamination in this laminated composite. As discussed above, the results also seem to suggest that τ_{xz} is independent of L_2. Further work is needed to clarify this aspect.

SUMMARY AND CONCLUSIONS

In summary, both experimental and numerical investigations were carried out in this work to study the low velocity impact delamination in the $[0_5, 90_5, 0_5]$ CF/PEEK laminate. The contact force history was recorded by the impact tester, and the
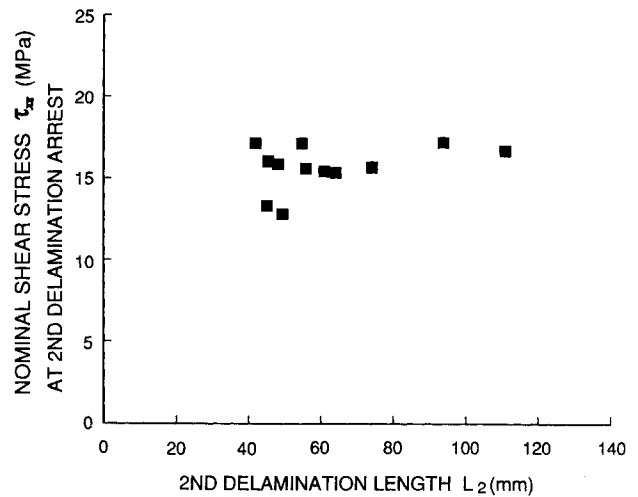
resulting delamination area was detected by the X-radiography and thermal deply technique. The impact force history was fed to a finite element model for calculating the dynamic stress response of the intact laminate. Fractography of the delamination surface was also studied.

The impact damage mechanisms in thermoplastic CF/PEEK composite are the same as in epoxy-based composites. The linear dependence of total delamination area on impact energy is also valid. CF/PEEK composite is superior to Kevlar/epoxy and graphite/epoxy composites in impact delamination resistance. For the crossply laminate, impact delamination is apparently controlled by a Mode II interlaminar fracture mechanism, and a close resemblance exists between the nominal interlaminar shear stress field and the delamination growth. The crack-arrest toughness seems to be a good candidate for the prediction of the impact induced delamination in this composite.

ACKNOWLEDGMENTS

NOMENCLATURE

L	= Length of delamination in the fiber direction of the lower ply.
W	= Width of delamination in the transverse direction to L.
E_{11}	= In-plane longitudinal Young's module.
E_{22}	= In-plane transverse Young's module.
G_{12}	= In-plane shear module.
ν_{12}	= In-plane longitudinal Poisson's ratio.
ρ	= Mass density.
σ_y^{cr}	= In-plane transverse tensile strength.

$\sigma_x, \sigma_y, \tau_{xy}$ = In-plane stresses.

τ_{xz}, τ_{yz} = Out-of-plane (transverse) shear stresses.

G_{IIa} = Mode II static strain energy release rate at crack arrest.

K_{II} = Mode II stress intensity factor.

Y = Geometry function in stress intensity factor calculation.

τ_0 = Nominal shear stress.

a = Crack length.

x, y, z = Cartesian coordinates.

REFERENCES

1. "Foreign Object Impact Damage to Composites," ASTM STP 568, Philadelphia (1975).
2. J. G. Williams and M. D. Rhodes, in "Composite Materials: Testing and Design" (Sixth Conference), ASTM STP 787, I. M. Daniel, ed., 450 (1982).
3. R. L. Ramkumar, in "Long-Term Behavior of Composites," ASTM STP 813, T. K. O'Brien, ed., 116 (1983).
4. N. Cristescu, L. E. Malvern, and R. L. Sierakowski, in "Foreign Object Impact Damage to Composites," ASTM STP 568, Philadelphia, 159 (1975).
5. S. P. Joshi and C. T. Sun, *J. Compos. Mater.*, **19**, 51 (1985).
6. F.-I. Chang, H. Y. Choi, and S.-T. Jeng, *SAMPE J.*, **26** (Jan/Feb), 18 (1990).
7. J. E. Masters, in "Fractography of Modern Engineering Materials: Composites and Metals," ASTM STP 948, J. E. Masters and J. J. Au, eds., 238 (1987).
8. N. Takeda, R. L. Sierakowski, C. A. Ross, and L. E. Malvern, *Exp. Mech.*, **22**, 19 (1982).
9. D. Liu, *J. Compos. Mater.*, **22**, 674 (1988).
10. E. G. Guynn and T. K. O'Brien, in Proc. AIAA/ASME/SAE 26th Structures, Structural Dynamics, and Materials Conference, Orlando, Fla., (1985).
11. P. H. Chen, Z. Shen, Q. Q. Shi, and H. Wang, in 5th National Conference on Composites, Xian, China (1988).
12. S. R. Swanson and H. G. Rezaee, *Compos. Sci. Technol.*, **38**, 43 (1990).
13. B. V. Sankar, *J. Reinforced Plast. Compos.*, **8**, 458 (1989).
14. C. T. Sun and S. Rechak, in "Composite Materials: Testing and Design (Eighth Conference)," ASTM STP 972, J. D. Whitcomb, ed., 97 (1988).
15. C. T. Sun and S. Chattopadhyay, *J. Appl. Mech.*, **42**, 693 (1975).
16. R. L. Ramkumar and P. C. Chen, *AIAA J.*, **21**, 1448 (1982).
17. T. M. Tan and C. T. Sun, *J. Appl. Mech.*, **52**, 6 (1985).
18. C. T. Sun and J. K. Chen, *J. Compos. Mater.*, **19**, 490 (1985).
19. E. Dan-Jumbo, A. R. Leewood, and C. T. Sun, in "Composite Materials: Fatigue and Fracture, Second Volume," ASTM STP 1012, P. A. Lagace, ed., 356 (1989).
20. A. D. Curson, D. C. Leach, and D. R. Moore, *J. Thermoplast. Compos. Mater.*, **3**, 24 (1990).
21. C. Bernard, J. Denault, J. Dufour, and T. Vu-Khanh, *IMI/NRCC Report* 89RT-103-865-C.
22. C. A. Ross, L. E. Malvern, R. L. Sierakowski, and N. Taketa, in "Recent Advances in Composites in the United States and Japan," ASTM STP 864, J. R. Vinson and M. Taya, eds., 355 (1985).
23. N. Takeda, R. L. Sierakowski, and L. E. Malvern, *SAMPE Quarterly*, **12**, 9 (1981).
24. N. Takeda, R. L. Sierakowski, and L. E. Malvern, *J. Compos. Mater.*, **15**, 157 (1981).
25. J. E. Grady and C. T. Sun, in "Composite Materials: Fatigue and Fracture," ASTM STP 907, H. T. Hahn, ed., 5 (1986).
26. S. M. Freeman, in "Composite Materials: Testing and Design (Sixth Conference)," ASTM STP 787, I. M. Daniel, ed., 50 (1982).
27. P. O. Sjoblom, J. T. Hartness, and T. M. Cordell, *J. Compos. Mater.*, **22**, 30 (1988).
28. L. E. Malvern, C. T. Sun, and D. Liu, in "Composite Materials: Fatigue and Fracture, Second Volume," ASTM STP 1012, P. A. Lagace, ed., 378 (1989).
29. D. Liu, *J. Reinf. Plast. Compos.*, **9**, 59 (1990).
30. H.-Y. T. Wu and G. S. Springer, *J. Compos. Mater.*, **22**, 533 91988).
31. *ABAQUS User's Manual*, Version 4.8, Hibbitt, Karlsson & Sorensen, Inc. (1989).
32. J. M. Whitney and N. J. Pagano, *J. Appl. Mech.*, **37**, 1031 (1970).
33. J. N. Reddy and E. J. Barbero, *Int. J. Numer. Methods Eng.*, **28**, 2275 (1989).
34. R. A. Chaudhuri, *Compute. Struct.*, **23**, 139 (1986).
35. N. J. Pagano and S. J. Hatfield, *AIAA J.*, **10**, 931 (1972).
36. N. M. Newmark, *J. Eng. Mech. Div. in Proc. American Society Civil Engineers*, 67 (1959).
37. T. J. Chapman, J. W. Gillespie, Jr., R. B. Pipes, J-A. E. Manson, and J. C. Seferis, *J. Compos. Mater.*, **24**, 616 (1990).
38. G. Jeronimidis and A. T. Parkyn, *J. Compos. Mater.*, **22**, 401 (1988).
39. "Property Data of Aromatic Polymer Composites," APC-2/Hercules Magnamite AS4 Carbon Fiber, ICI, Inc.
40. G. J. Becht and J. W. Gillespie, Jr., *Polym. Compos.*, **10**, 293 (1989).
41. T. Vu-Khanh, *Polym. Compos.*, **8**, 331 (1987).
42. T. Vu-Khanh, R. Langlois, and R. Gauvin, in *Proc. ICCM-7*, Y. Wu, Z. Gu, and R. Wu, eds., Guangzhou, China (1989).